# GOLD Observations of Equatorial Plasma Bubbles Reaching Mid-Latitudes During the 23 April 2023 Geomagnetic Storm

**Deepak Kumar Karan[1], Carlos R. Martinis[2], Richard W. Eastes[1], Robert E. Daniell[3], William E. McClintock[1] and Chao-Song Huang[4]**

[1]Laboratory for Atmospheric and Space Physics, University of Colorado, Boulder, CO, USA
[2]Center for Space Physics, Boston University, MA, USA
[3]Ionospheric Physics, Stoughton, MA, USA
[4]Space Vehicles Directorate, Air Force Research Laboratory, Albuquerque, NM, USA

Corresponding author: Deepak Kumar Karan (Deepak.Karan@lasp.colorado.edu)

**Key Points:**

- Maximum poleward shift (~11°) of EIA crests was observed between ~15°W-5°W Glon
- Reversed C-shape Equatorial Plasma Bubbles (EPBs) extended to ~±36° Mlat (~40°N and ~30°S Glat) with apex altitudes reaching ~4000 km
- Shear in EPBs zonal drifts is formulated as a function of magnetic apex heights based on their tilts.

**Key Words:** NASA GOLD mission, Geomagnetic storm, Equatorial Ionization Anomaly, Equatorial Plasma Bubble, Nighttime ionosphere, Extreme EPB, Super Plasma Bubbles

## Abstract

A coronal mass ejection erupted from the Sun on 21 April 2023 and created a G4 geomagnetic storm on 23 April. NASA's Global-scale Observations of the Limb and Disk imager observed bright Equatorial Ionization Anomaly crests at ~25° Mlat, ~11° poleward from their average

locations, computed by averaging the EIA crests during the previous geomagnetic quiet days (18 to 22 April) between ~15°W-5°W Glon. Reversed C-shape Equatorial Plasma Bubbles were observed reaching ~±36° Mlat (~40°N and ~30°S Glat) with apex altitudes ~4000 km and large westward tilts of ~52°. Using GOLD's observations EPBs zonal motions are derived. It is observed that the EPBs zonal velocities are eastward near the equator and westward at mid-latitudes. Model-predicted prompt penetration electric fields indicate that they may have affected the postsunset pre-reversal enhancement at equatorial latitudes. Zonal ion drifts from a defense meteorological satellite program satellite suggest that westward neutral winds and perturbed westward ion drifts over mid-latitudes contributed to the observed latitudinal shear in zonal drifts.

## Plain Language Summary

A severe geomagnetic storm occurred on 23 April 2023. The effects of the storm on the nighttime equatorial and mid-latitude ionosphere are investigated using NASA's Global-scale Observations of the Limb and Disk measurements. GOLD observed bright, widely separated Equatorial Ionization Anomaly crests between ~15°W-5°W Glon. Extreme Equatorial Plasma Bubbles reaching mid latitudes at ~40°N and ~30°S Glat with apex altitudes of ~4000 km at the magnetic equator were observed over these longitudes. The EPBs velocities were eastward at low latitudes, between the EIA crests, and reversed to westward near mid-latitudes. At mid-latitudes EPBs showed westward tilts that were larger than previous observations during similar geomagnetic conditions.

## 1 Introduction

The Equatorial Ionization Anomaly (EIA), also referred to as the Appleton Anomaly, is a consistent ionospheric feature at equatorial and low latitudes (Appleton, 1946). It's caused by interactions between equatorial F region eastward electric fields and horizontal northward magnetic fields, resulting in an upward drift over the magnetic equator. This vertical drift causes the ionospheric plasma to ascend to higher altitudes and diffuse along magnetic field lines towards lower latitudes, a phenomenon known as the fountain effect (Hanson and Moffet, 1966). Consequently, the plasma density exhibits a double-peaked structure in the latitudinal distribution of the F region, with two maxima around 15°-20° north and south of the magnetic equator and a minimum at the equator. This distinctive pattern, characterized by crests on each side and a trough

over the magnetic equator, defines the EIA. In the same ionospheric region, Equatorial Plasma Bubbles (EPBs) are also observed. Following sunset, the lower side of the ionosphere undergoes faster recombination due to increased ion-neutral collision frequencies compared to the upper side. Additionally, the equatorial vertical drift increases shortly after sunset, known as the Pre-Reversal Enhancement (PRE), causing an upward movement of the ionosphere. This results in a sharp gradient in electron density, leading to the Rayleigh-Taylor Instability (RTI). Perturbations in depleted or enhanced density at the bottom side of the ionosphere move upward or downward, respectively (Kelley, 2009). These depleted plasma density regions, or depletions, alter vertical electron density distributions, giving rise to plasma irregularities known as equatorial plasma bubbles (EPBs) in airglow ionospheric images.

The characteristics and variations of the EIA depend on several factors, including neutral winds, tides, electric fields, magnetic declination, PRE, ion production and loss rates, and the subsolar point location (Eastes et al., 2023 and references therein). EPBs are linked to factors like neutral winds, electric fields, conductivities, and plasma density, as noted in Karan et al., (2020, 2023b). Geomagnetic disturbances alter the above factors affecting the EIA and EPBs, causing changes in their characteristics.

Geomagnetic storms alter winds and electric fields through prompt penetration electric field (PPEF) (Kelley et al., 2003) and disturbance dynamo electric fields (DDEF) (Blanc and Richmond, 1980; Fejer et al., 1979), thereby changing the EIA morphology (Abdu et al., 1991, 1995; Balan et al., 2018). Sometimes during nights, the electron density in the EIA crests latitudes increases due to the penetration of an eastward disturbance electric field (Takahashi et al., 1987; Balan et al., 2018). Furthermore, storm-generated equatorward winds can move up ionospheric layers to higher altitudes, where recombination occurs more slowly, resulting in larger EIA peak densities that decay more slowly (Lin et al., 2005). During storms, the EIA may expand polewards, displacing the crests to mid-latitudes. Karan et al., (2023a) observed an $8^{o}$-$10^{o}$ poleward shift of post-sunset EIA crests during a storm, attributed to an enhanced PRE driven by an increase in eastward PPEF, corroborated by ionosonde measurements that showed an increase in the height of the peak electron density, hmF2.

Like the changes in the EIA's behavior during geomagnetic storm time, EPB's occurrence and morphology are also impacted. Geomagnetic storms can either promote or hinder the formation of EPBs (Aarons et al., 1991; Abdu et al., 1995; Cherniak & Zakharenkova, 2022; Martinis et al., 2005; Kil et al., 2016; Patra et al., 2016). During some storms, the PRE is intensified, causing EPBs to ascend to higher apex altitudes with field lines reaching latitudes around ~30-40$^{o}$ Mlat (Aa et al., 2018, 2019; Martinis et al., 2015; Rajesh et al., 2022; Huba et al., 2023; Sousasantos et al., 2023). In the equatorial F region during geomagnetically quiet conditions, the nighttime zonal plasma motion is eastward, but it is slower at higher and lower altitudes. This causes the EPBs to move slower at higher and lower apex altitudes. Thereby, the EPB appears to be a reversed C-shaped (Karan et al., 2020; 2023a; Kil et al., 2009; Martinis et al., 2003; Zalesak et al., 1982). Using data form an all-sky imager at Ascension Island (~14$^{o}$W Glon, ~8$^{o}$S Glat, ~18$^{o}$S Mlat), Mendillo and Tyler (1983) formulated a relationship between the EPBs westward tilt and the local time, showing that the tilt increased as the night progressed. During geomagnetic storms the wind pattern changes, causing changes in the shape of EPBs. Zonal drifts of the plasma at low and mid latitudes can become westward due to the westward neutral winds (Sutton et al., 2005), equatorward expansion of subauroral ion drifts (Ferdousi et al., 2019), or the influence of traveling ionospheric disturbances (TIDs) (Aa et al., 2019). These westward drifts of plasma can increase the EPBs' westward tilt, but this has not been quantified under perturbed geomagnetic conditions.

In this work, we investigated the poleward expansion of EIA and reversed C-shape EPBs extending to mid-latitudes between ~15$^{o}$W-5$^{o}$W Glon during the 23 April 2023 geomagnetic storm, using NASA's Global-scale Observations of the Limb and Disk (GOLD) images. Relationships between the EPB's zonal drifts with apex altitudes are established.

## 2 Data

This study utilizes nighttime partial disk images from the GOLD imager, situated in a geostationary orbit at 47.5$^{o}$W, featuring two identical and independent channels (A and B, CHA and CHB hereafter), capturing FUV wavelengths (~132-162 nm). Nominal operations and observations commenced on 9 October 2018. The primary objectives of GOLD are twofold: (i) to investigate the response of Earth's ionosphere-thermosphere system to geomagnetic storms, solar

activity, and atmospheric waves, and (ii) to explore the formation and development of ionospheric plasma irregularities. GOLD measures the emission rate integrated along the line of sight. One of GOLD's strengths is its ability to observe the longitudinal regions of the South America, the Atlantic, and Western Africa, offering a unique opportunity to observe the spatial-temporal evolution of various features of the ionosphere and thermosphere that are visible to GOLD. It conducts entire disk observations, limb scans, and occultations which have resulted several interesting findings about the ionospheric and thermospheric behavior during different geophysical conditions (Aa et al., 2022; 2023; Aryal et al., 2023; Cai et al., 2023; Gan et al., 2023; Laskar et al., 2024; ). The instrument and its observations are detailed in Eastes et al., (2017, 2019, 2020) and McClintock et al., (2020). The nighttime OI 135.6 nm emission is produced by recombination of atomic oxygen ions and electrons in the Earth's ionosphere. Since the emission rate varies approximately as the square of the electron density, it maximizes at the peak F layer which is assumed to be 300 km. GOLD takes images across the American, Atlantic, and West African longitudinal sectors between 19 and 22 LT.

Solar wind parameters, geomagnetic indices, and modeled equatorial ionospheric eastward electric field (EEF) (Manoj and Maus, 2012) are used to provide context for the GOLD observations. The EEF is continuously forecasted in real-time by leveraging solar wind data from the Deep Space Climate Observatory (DSCOVR) and NASA/ACE spacecraft, sourced through NOAA's Space Weather Prediction Center. Employing a transfer function model, the application predicts EEF fluctuations based on solar wind data, while incorporating a climatological model to accommodate variations in EEF during quiet days. Zonal ion drifts from a Defense Meteorological Satellite Program (DMSP) satellite are compared with GOLD-inferred EPB zonal drifts.

## 3 Results

Figure 1 presents GOLD observations of the EIA and EPBs on the storm night, 23-24 April 2023. Images are selected to cover all the longitudes and to avoid repetition at similar longitudes. All the images during 23 April 20:10 UT to 24 April 00:25 UT are available as Movie-M1 in the supporting information. The images in the top row (panels A-D) illustrate that the EIA crests are brighter, and EPBs, represented by dark bands extending through the EIA crests, are observed at

longitudes to the east of ~ 30° W, while no EPBs are seen to the west of ~30° W (panels E-H). All the EPBs exhibit significant westward tilts on both hemispheres.

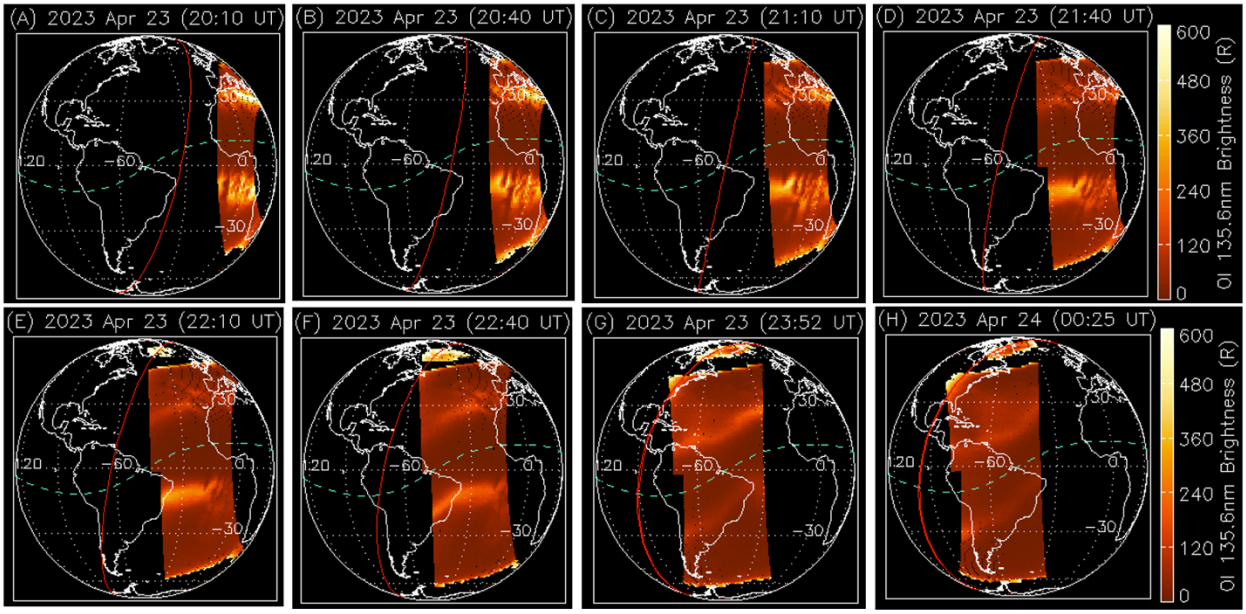


Figure 1. Nighttime 135.6 nm images captured by the GOLD imager on April 23-24, 2023. Highlighted are selective images covering all longitudes monitored by GOLD. The dashed green line and solid red line represent the geomagnetic equator and the sunset terminator, respectively.

The geomagnetic conditions on 22-23 April 2023 are shown in Figure 2. Solar wind parameters are in panels A (magnetic field IMF Bz and electric field IEF Ey) and B (solar wind proton density and speed). Panel C displays the equatorial geomagnetic index (SYM-H). The thick red line at the bottom of panel C indicates the times of GOLD's observations. The main phase of the storm commenced around 09:00 UT on 23 April and persisted until ~05:00 UT, when SYM-H reached a minimum value of ~ -220 nT. About 11 hrs after the initiation of the main phase, GOLD nighttime observations started as the SYM-H reached a minimum value of ~175 nT. At about 18 UT, Bz changed suddenly (density and speed also changed), reaching ~22 nT and maintaining this level for ~2 hrs. The 18-20 UT time range corresponds to post-sunset times in the longitudes ~15°W-5°E. These conditions led to the penetration of an E-field into equatorial latitudes.

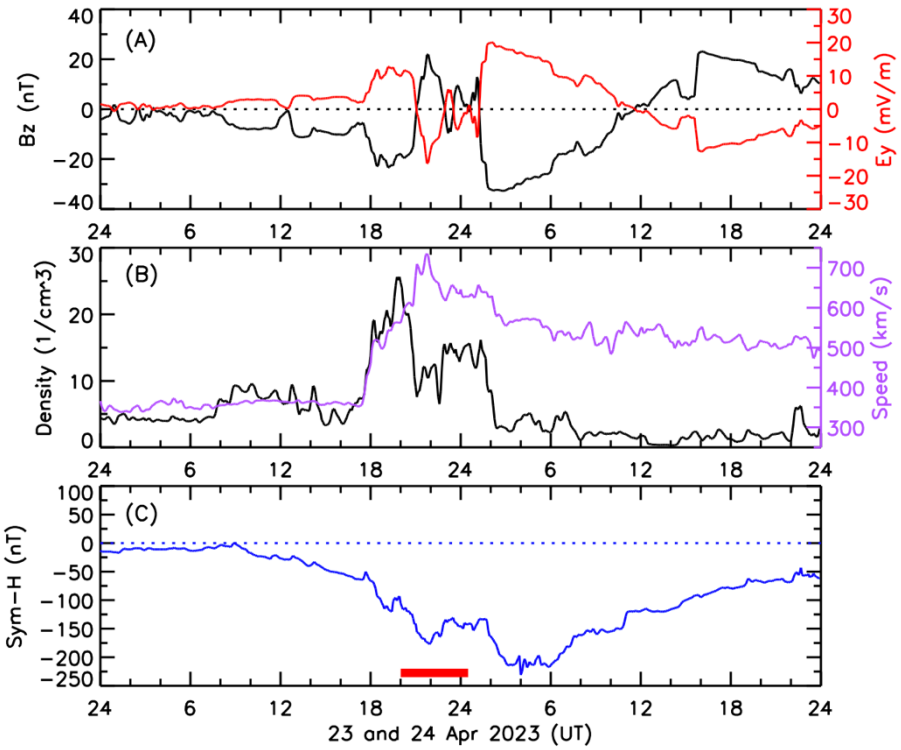


Figure 2. Solar wind parameters and geomagnetic indices on 23-24 April 2023. (A) IMF Bz and IEF Ey; (B) proton density and plasma flow speed, and (C) Sym-H. The thick horizontal red line indicates the timing of GOLD observations.

To investigate the geomagnetic storm's effect on the EIA crests latitude values, we obtained the crests latitudes on the storm night (23-24 April). GOLD's captured images are transformed into quasi-dipole geomagnetic coordinates, using the International Geomagnetic Reference Field scalar potentials. These remapped images allow us to analyze variations in brightness at 135.6 nm concerning magnetic latitudes, spaced at 2° magnetic longitude intervals. Peaks in brightness along latitudinal variations indicate the positions of EIA crests. By applying this approach to all images, we derive the latitudes of the EIA crests. Subsequently, we calculate the average and standard deviation of the latitudes for both the North (N) and South (S) crests which is shown in Figure 3 panel A. This methodology is detailed in the work by Eastes et al. (2023). Larger standard deviations, particularly near ~15°W, are a result of increased uncertainties during the calculation of EIA crests locations in the presence of EPBs. The red and blue solid lines indicate the average EIA crests latitudes during the previous geomagnetic quiet days (18 to 22 April). On the storm night, the EIA crests extended furthest between ~15°W-5°W Glon, with the N and S crests at ~27° and ~25° Mlat, respectively. Panel B illustrates the differences between the

storm night EIA crest latitudes and the quiet time average values. Maximum poleward shifts of ~11° and 9° in the N and S EIA crests were observed between ~15°W-5°W Glon.

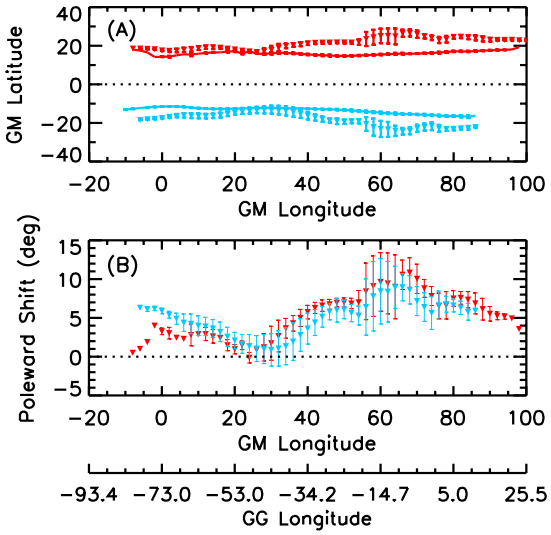


Figure 3. (A) EIA crests latitudes, North (red) and South (blue). 23 April shown as dashed lines and quiet time average as solid lines; (B) Relative shifts in EIA crests latitudes on 23 April 2023 compared to quiet time average with uncertainties.

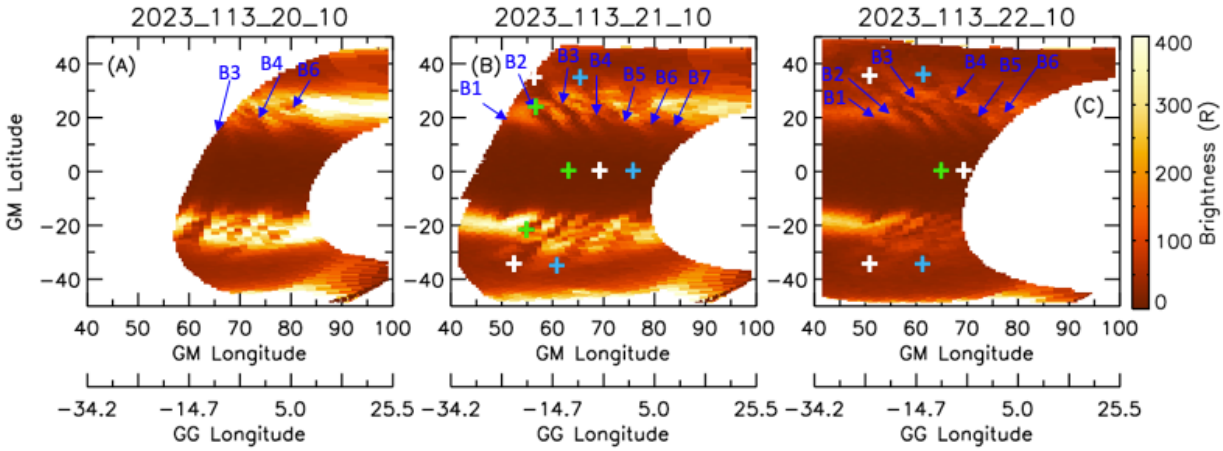


Figure 4. (A), (B), (C) combined CHA (N-hemisphere) and CHB (S-hemisphere) images at 20:10, 21:10, and 22:10 UT, respectively.

Panels A, B, and C in Figure 4 show the combined CHA and CHB images in quasi-dipole (QD) coordinates (Laundal and Richmond, 2017) at 20:10, 21:10, and 22:10 UT, respectively, encompassing seven EPBs (marked as B1 to B7) observed during this night. These EPBs exhibit

a westward tilt relative to the magnetic meridian and extend poleward through and beyond the EIA crests. The foot points of B3 and B4 (indicated by white and cyan '+' symbols, respectively) extended beyond ~±36° Mlat (~40°N and ~30°S Glat) (panels 4B and 4C), implying structures with apex altitudes exceeding ~4000 km. Magnetic field lines were traced using the IGRF-13 model (Alken et al., 2021). EPB B2 appeared to merge with B3 at latitudes beyond the EIA crest (panel 4C). The time sequence of the behavior of EPBs is shown as a movie Movie-M2 in the supporting information. All seven EPBs were situated within ~15°W-0° Glon (~60° to 75° Mlon). For a clear view of EPB locations near the magnetic equator, where the brightnesses were lower compared to the EIA crests, panels 4A-C were replotted with a lower brightness scale in Figure S1 in the supporting information. The bubbles separation at the equator was ~5°, which increased to ~8° at the EIA crests latitudes.

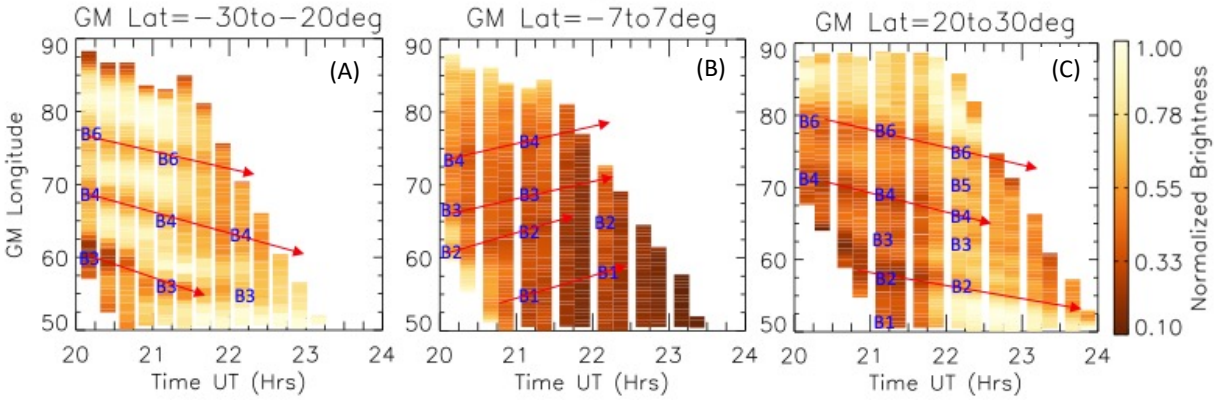


Figure 5. (A), (B), (C) longitudinal variations of normalized brightness obtained at different times as keograms for 30°-20°S, 7°S to 7°N and 20°-30°N latitude ranges, respectively.

The westward tilt angles of B2 and B3 at 22:10 UT are ~42° at ~16° Mlat, and ~52° at ~30° Mlat. These tilts can be related to altitudinal/latitudinal shears in the zonal plasma drifts. Thus, we tracked the EPBs drifts at several latitudes. The method for deriving EPBs' drift velocity is detailed in Karan et al., (2020). EPBs were moving eastward near equatorial and low latitude regions and westward at latitudes higher than ~±20° Mlat. Keograms in Figure 5 illustrate this behavior. Three magnetic latitude ranges, 30°-20°S, 7°S-7°N, and 20°-30°N were selected. In an image (at a fixed UT), within 30°-20°S latitude range, the brightness at each longitude is averaged to obtain the longitudinal variations of the brightnesses at that UT. To enhance visibility of the EPBs against the varying background brightness, the brightness array was normalized to a maximum of 1. This

process was repeated for all the images, and the results were coplotted as a keogram in panel 5A. Same method is followed to obtain keograms for 7°S-7°N and 20°-30°N, shown in panels 5B and 5C, respectively. Different time gaps between the longitudinal stamps in the keograms are due to varying latitudinal coverage of the images. EPBs longitudinal shifts are shown by red arrows (drawn by hand to aid viewer's eyes). The average zonal drifts of all EPBs during the observation periods is 120±15 m/s eastward within the 7°S-7°N latitudes (panel 5B), whereas within the latitude range of 20°-30°N and 30°-20°S, they reversed and are 70±3 and 85±4 m/s westward, respectively.

## 4 Discussion

On 23 April 2023, we observed maximum poleward shifts of ~11° in the northern and ~9° in the southern hemisphere EIA crests in between ~15°-5°W Glon. In the same longitude sector, reversed C-shape EPBs extending poleward beyond ±36° Mlat (~40°N and ~30°S Glat) were detected. The poleward shifts of the EIA crests are similar to the ones reported by Karan et al., (2023a) at a larger longitude range of ~65°-35°W Glon, during a co-rotating interaction region geomagnetic storm weaker than the coronal mass ejection one on 23 April 2023. The ionospheric response in that study showed that the peak altitude of the ionospheric hmF2 layer increasing over those longitudes. The number of EPBs also increased, as on 23 April 2023, but now the morphology shows extreme characteristics.

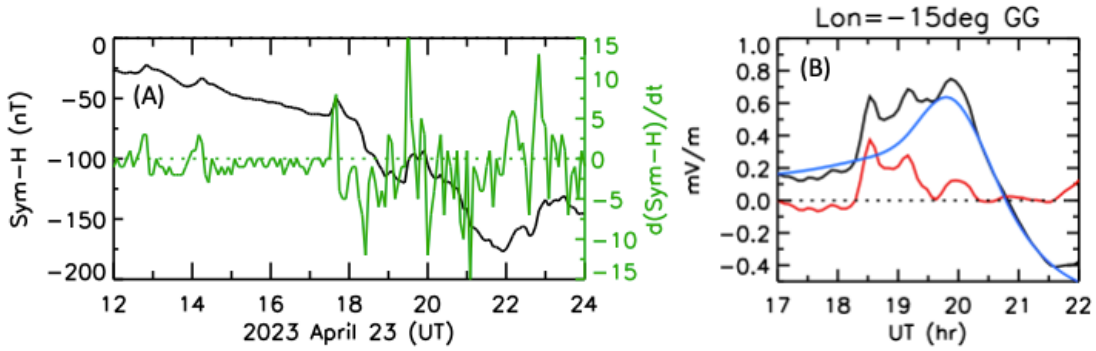


Figure 6. (A) Sym-H index in black and d(Sym-H)/dt in green during 12 to 24 UT on 23 April; (B) modeled total zonal electric field (black), PPEF (red), and quiet time electric field (blue) at 15°W Glon on 23 April.

The maximum poleward shifts of the EIA crests latitudes in between ~15°-5°W Glon (Figure 3) is likely due to an enhanced PRE (Abdu et al., 1991; Balan et al., 2018), This enhancement could be due to a penetration electric field. Sym-H and its rate of change, d(Sym-H)/dt, are shown in panel A of Figure 6. The rate of change of Sym-H showed a large negative excursion at ~18:30 UT with a maximum value of ~ -12 nT/5 min (~ -144 nT/hr). The sudden increase of IEF Ey at ~18UT (panel 2A) and the sharp decrease in Sym-H at ~18-19 UT suggest a prompt penetration of an eastward electric field into the equatorial and low latitudes at this dusk sector (~15°W Glon) due to under-shielding conditions (Fejer et al., 1979; Kelley, 2003; Martinis et al., 2005). In the absence of electric field measurements over this longitude sector, the electric field model developed at Geomagnetism, CIRES (Cooperative Institute for Research in Environmental Sciences) (Manoj and Maus, 2012) was used. This model has been applied in other studies (Aa et al., 2019; Karan et al., 2023a; Spogli et al., 2021). Panel B shows the quiet time, prompt penetration (PPEF), and total electric fields in blue, red, and black lines, respectively. PPEF between ~18:15-20:15 UT contributed to ~2 hr extended PRE (peak value ~0.7 mV/m at ~20 UT). The maximum poleward shift in the EIA crests latitudes observed an hour after the peak PRE could be due to the transport time of plasma from equator to EIA crests (Karan et al., 2016, Karan and Pallamraju, 2020). A zonal electric field of ~0.7 mV/m produces an upward drift of ~32 m/s at this longitude. The PRE duration was ~1hr in the previous quiet days. For the mid latitude EPBs reported by Aa et al. (2019), the model total electric field was 0.9 mV/m with a duration of ~1hr. The longer duration PRE in the present case (~2 hrs) could have enhanced plasma drift shifting the EIA crests further poleward.

The long-duration PRE is also an important factor for the generation and maximum altitude of the EPBs. At 20:10UT, just one hour after the sunset, GOLD detected a well-developed EPB B3 already reaching an apex altitude of ~2000 km (Panel A in Figure 4). This implies that the EPBs had upward drifts of ~500 m/s, an unusually large value that, has rarely been reported in the past. For example, upward drifts ~1200 m/s were measured by Abdu et al. (2008), between 100-1000 m/s by Aggson et al., (1992), and ~1200 m/s by Hysell (1994). While we have no means to effectively measure the upward drift, some inferences can be made from the poleward motion of EPBs as observed by GOLD. By measuring the poleward motion of B1, B2, B3, and B4 between 18°-24° Mlat an average speed of ~130 m/s is obtained, which is similar to ~110 m/s reported in

Martinis et al., (2015) who investigated EPBs reaching midlatitudes. This poleward drift can be interpreted as a vertical drift near the magnetic equator with an eastward electric field of ~3.3 mV/m. In the present case, the long-duration PRE could have moved the F layer to high altitudes and caused the generation of EPBs with deep density depletion.

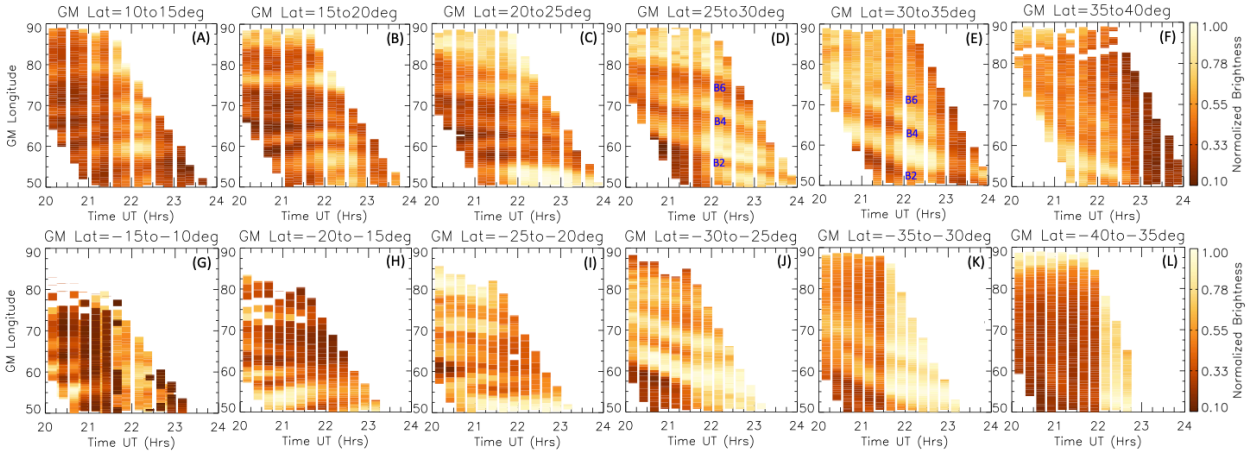


Figure 7. Same as Figure 5 (Panels A-C but at 5º latitude ranges. The transition in the EPBs eastward motion at equatorial and low latitudes to westward at mid latitudes can be seen close to ±20º Mlat, between panels B-C and H-I.

Along with the expansion of the EPBs to higher altitudes/latitudes, their drift directions changed from eastward (near the magnetic equator) to westward (at latitudes higher than ~±20º Mlat) (Figure 5). The latitude where the EPB drifts reversed can be investigated by plotting the keograms in 5º latitude ranges, shown in Figure 7. Panels 7A (10º-15ºN) and 7G (10º-15ºS) show that, at ~ 22 UT EPB's longitude shift with time becomes flat when compared to the variation within 7ºS to 7ºN latitude range (panel 5B). This indicates that the EPBs drifts slowed down from equatorial to low latitude regions. The reverse in EPBs' longitude shift direction with time around ±20º Mlat indicates that EPBs motion changed from eastward to westward close or below this latitude.

The reduction and reversal of eastward drifts from low to midlatitudes has usually been related to ionospheric disturbance dynamo (Blanc and Richmond, 1980; Fejer et al., 1979; Sutton et al., 2005). Recently, Huang et al., (2021) show subauroral polarization streams (SAPS) effects reaching low latitudes. Figure 8 displays the net change (or difference) in zonal ion drifts between the storm and a quiet day (22 April), used as reference, as measured by DMSP F17. Panel 8a shows

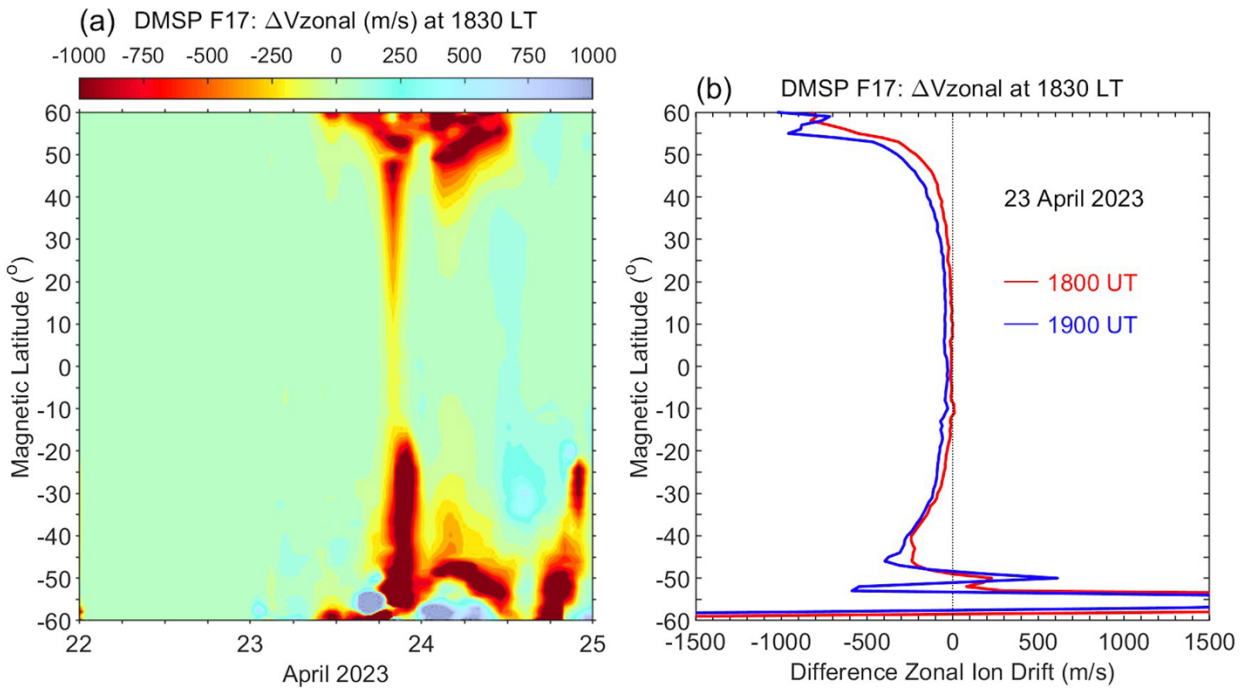


Figure 8. (a) Difference zonal ion drifts measured by the DMSP F17 satellite at ~18:30 LT considering April 22 as a reference and (b) Latitudinal profile of the difference zonal ion drifts at 18 and 19 UT.

the difference in zonal ion drifts between 23 and 22 April. DMSP F17 observations at 18:30 LT at certain longitudes is interpolated for other UTs. Panel 8b shows the values at 18 and 19UT, which correspond to longitudes ~7.5ºE and ~7.5ºW on Apr 23, where westward tilted EPBs were observed. On the storm day, reductions of the zonal ion drifts ~30 m/s, ~60 m/s, and ~100 m/s at ~0º, ~15º, and ~30º Mlat, respectively, were observed. The westward drifts of ~800 m/s and ~500 m/s at subauroral latitudes of ~55º N and ~55º S indicate SAPS effects, potentially penetrating to middle and low latitudes, contributing to the westward drifts measured. Utilizing GOLD observations, we calculated the difference in EPBs' zonal drifts between 23 and 22 April. A reduction of ~90 m/s in EPBs' zonal drifts was identified at ~15º Mlat and ~7ºW Glon (location of B3) around 19 UT, result that is similar with the DMSP reduction observed at ~15º Mlat (60 m/s). Thus, the reversal of EPBs' zonal drifts, transitioning from eastward at low latitudes to westward at middle latitudes, as observed by GOLD, agrees with the latitude profile of the difference in zonal plasma drifts measured by DMSP.

As mentioned earlier, the EPBs appeared as reversed C-shape structures, related to their westward tilts. GOLD measures EPBs in a latitude and longitude plane, off the magnetic equator, at a fixed height of 300 km. Focusing on bubble B3 the tilt seems to change with latitude. At 22:10 UT around 35°N Glat (~30° Mlat) and 25°N Glat (~16° Mlat) the tilts are ~52° and ~42° westward. Considering that the magnetic declination at these locations are ~5° and 1.5°, then B3 is tilted ~47° and ~40.5° with respect to (w.r.t.) the magnetic meridian. Bubble B2 shows a tilt of 40°, or ~37° w.r.t. the magnetic meridian. In comparison, the westward tilt w.r.t. magnetic meridian from Aa et al., (2019) were ~25° and ~11° at similar magnetic latitudes and from Martinis et al., (2015), it was ~22° at ~30° Mlat. Geomagnetic conditions were similar, with Sym-H reaching ~ -110 nT in these studies. Because EPBs exhibit a plasma flux-tube nature along the magnetic field lines, an alternative method for measuring tilt involves mapping them into the magnetic equatorial plane. This representation depicts an EPB in an altitude-magnetic longitude plane, where altitude corresponds to the field line's apex height, and is linked to the magnetic latitude at the field line's footpoint. In this plane, B3 reaches ~36° Mlat with a break or kink in the shape of the bubble between ~24-25 ° Mlat. The westward tilt for the upper portion of B3 is ~25 ° and for the lower part ~32 °. B2 reaches ~25° Mlat with a westward tilt of ~34°.

Mendillo and Tyler (1983) (M&T) used this approach to quantify the EPBs westward tilt (W) as a function of local time as observed from Ascension Island using ground-based imaging. The apex altitudes they observed ranged from 400-1200 km. For the relatively geomagnetic quiet conditions prevalent during their observations, they found:

$$W = 0.15\ (LT-18.3) \qquad (1)$$

W is the westward shift in degrees of magnetic longitude per 100 km in apex altitude. Applying this formula to EPBs B2 and B3 of Figure 4, we obtain W = 0.43. Expressed as the angle between the orientation of the EPB and the magnetic meridian, this becomes 23°.

We next compare this result with the measured tilt values of B2 and B3. At 20° Mlat B3 has $W_{B3l} = 0.63$ (corresponding to a tilt angle of 32°), while at 30° Mlat B3 has $W_{B3u} = 0.47$ (corresponding to 25°). For B2, which does not extend much past 25° Mlat, $W_{B2} = 0.67$ (corresponding to 34°). Since the GOLD observations occurred during a geomagnetic storm, it is not surprising that the westward tilts exceed those observed by M&T. Both studies found EPBs

with westward tilts. Under storm conditions, however, we observe nighttime zonal drifts at low and mid latitudes that display a reduction or even a reversal of the typical eastward motion to westward. Consequently, EPBs observed during storm conditions may exhibit a more 'compressed' reversed C-shape, which is precisely what GOLD is measuring.

If the westward tilt increases linearly following equation (1), M&T obtained an expression for the altitude dependence for an effective westward drift, or reduction in the overall eastward drift, V'(h) as

$$V'(h) = 0.0464(1+h/R_E) \quad (2)$$

Where 0.0464, in (m/s)/km units, is the product of the slope, 0.15 (measured in degrees of magnetic longitude per 100 km vertical height) from (1), and a constant 0.31 (result of geometric factors used in the calculation). At 300 km V'(300) = 0.049 m/s/km. This value represents the shear in altitude of the zonal drifts from a height of 300 km. An eastward drift at 700 km apex height (12.5$^o$ Mlat) would lag the drift at 300 km by 0.049*(700-300) ~ 20 m/s. Using an imager with a field of view of ~ 47$^o$ located in Maui, Hawaii, Makela and Kelley (2002) applied the M&T approach to EPBs and obtained an average shear value of 0.05 m/s/km. But when they calculated the shear by computing the velocities obtained at each height, a value of 0.1 m/s/km was obtained. This discrepancy was not explained.

Figure 9 shows the calculated EPBs' average zonal drift velocities for each of the latitude ranges (as shown in Figure 7) as a function of apex altitudes (or magnetic latitudes). Figure 7c shows that the reverse in EPBs longitude shift direction with time occurred around ±20$^o$ Mlat. about 22 UT. So, EPBs westward drifts after 22 UT is considered for this latitude range. Below ~1500 km apex height the larger slope (compared to heights above 1500 km) indicating a faster decrease (with latitudes) in the drift speeds. The average zonal drifts of the EPBs at apex altitudes close to 300 km (magnetic equator), 700 km, and 1000 km, are 120 m/s, 62 m/s, and 25 m/s, respectively. The transition from eastward to westward drift occurs around 1000 km (17.5$^o$ Mlat). According to (2) the transition height (where the lag is equal to ~120 m/s) should occur at ~2750 km, much higher than the height observed. Like the underestimation in the westward tilt W from (1), V' is also showing a weak altitude variation.

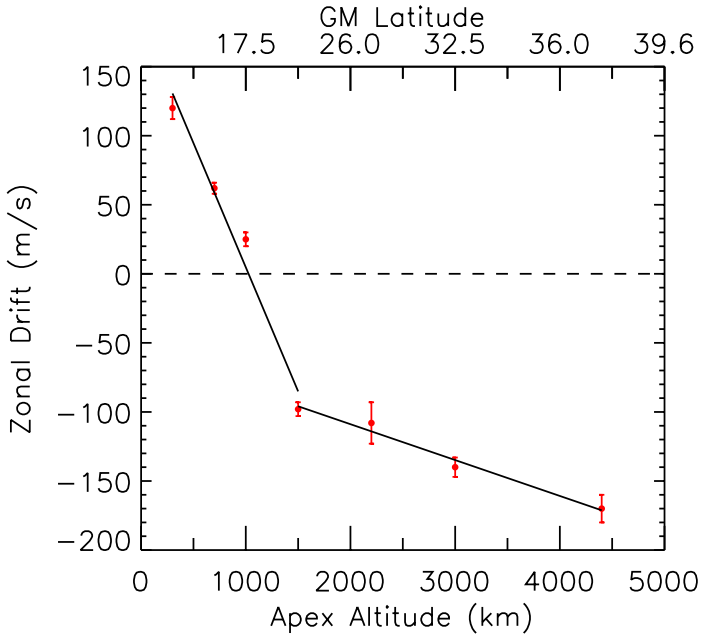


Figure 9. EPBs' average zonal drifts (m/s) for each latitude ranges (shown in Figure 7) with corresponding apex altitudes are shown. The transition from east to west occurred at ~1200 km (~20º Mlat).

The shear V'(300 km) for the GOLD data can be obtained from the slope of the fitted line to the data between 300 to 1500 km, shown in Figure 9. This slope is $V'_{GOLDl} = 0.179$ m/s/km. This shear can also be obtained by considering the average westward tilt of the EPBs measured in GOLD images. The westward tilt $W_{GOLD}$ at 20º Mlat can be calculated as the shift in magnetic longitude (5º) divided by the extent of the bubble (920 km), equal to – 0.63. When this value is multiplied by 0.31, a shear of 0.195 m/s/km is obtained, close to the slope of the fitted curve in Figure 9. This result indicates a good agreement between the shears obtained by the two methods, something that was not observed in the Makela and Kelley (2003) study.

With these new shear values (0.179 and 0.195), drifts at 1000 and 1500 km will lag the drift at 300 km by 112 (136) m/s and 192 m/s (234), respectively. The drifts at these heights will be 8 (-12) m/s and -70 (-114) m/s. The transition from eastward to westward occur at the observed height range of ~1000-1100 km. The upper part of B3 shows a different shear $V'_{GOLDu} = 0.026$ m/s/km, so the height variation of the drifts is weaker, as seen in Figure 8. We can summarize the results that relate westward tilts and height variation of zonal drifts of B3 as:

$W_{GOLDl} = 0.63$

$Vel_{\_l}$ = 185 m/s – 0.179*h for h < 1500 km (3)

and

$W_{GOLDu}$ = 0.47

$Vel_{\_u}$ = -57 -0.026*h for h > 1500 km (4)

Therefore, we obtained average expressions for the westward tilt and zonal drifts as a function of apex height. At lower altitudes, below ~1500 km, the height variation of zonal drifts is large, but above ~1500 km it proceeds at a smaller rate, but large westward drifts are measured. This indicates a different response of the ionosphere at low latitudes when compared to mid latitudes. One important point about the calculated drifts to note is that while geolocating the pixels if the height is 600 km rather than 300 km, then the derived velocity changes by < 5% which is not large enough to invalidate our conclusions.

## 5 Summary

This paper investigated the EIA and EPB characteristics as observed by the NASA GOLD imager during the 23 April 2023 geomagnetic storm. The perturbed geomagnetic conditions prevailing on that night were responsible for the emergence of EPBs characterized by significant westward tilts and substantial latitudinal shears in the zonal drift velocities. The key findings are:

(i) Maximum (~11°) poleward shifts of both EIA crests latitudes and reversed C-shape EPBs were observed at ~15°-5°W Glon. A modeled eastward PPEF lasted for ~2hrs and extended the PRE, moving plasma to higher latitudes.

(ii) EPBs reached beyond ±36° Mlat (~40° N and ~30°S Glat), implying structures with apex altitudes exceeding ~4000 km. EPBs showed westward tilts of ~52° at ~30° Mlat and ~42° at ~16° Mlat, higher than previously reported cases under similar geomagnetic conditions.

(iii) EPBs zonal drifts showed a strong latitudinal shear, with eastward drifts of 120±15 m/s over equatorial latitudes and westward drifts of 70±3 m/s at N and 85±4 m/s at S EIA crests.

(iv) Inferred poleward drifts obtained by GOLD images were used to estimate an effective eastward electric field of ~3.3 mV/m near the magnetic equator.

(v) The reversal of EPBs' zonal drifts as observed by GOLD, agrees with the latitude profile of the difference in zonal plasma drifts measured by DMSP.

(vi) We obtained expressions for the westward tilt of EPBs and the apex height (or magnetic latitude) dependence of their zonal drifts. Results show a linear variation up to ~1500 km (~22.5° Mlat), with smaller shears observed at higher latitudes.


## Acknowledgments

This research was supported by NASA contract 80GSFC18C0061 to the University of Colorado.


## Open Research

The GOLD data are available from the GOLD Science Data Center (https://gold.cs.ucf.edu/data/search/). The solar wind parameters and geomagnetic indices are taken from the NASA GSFC SPDF OMNI website (https://omniweb.gsfc.nasa.gov/form/omni_min.html). Model ionospheric electric fields are obtained from (https://geomag.colorado.edu/real-time-model-of-the-ionospheric-electric-fields).

## References


Aa, E., Huang, W., Liu, S., Ridley, A., Zou, S., Shi, L., Chen, Y., Shen, H., Yuan, T., Li, J., & Wang, T. (2018). Midlatitude plasma bubbles over China and adjacent areas during a magnetic storm on 8 September 2017. Space Weather, 16, 321– 331. https://doi.org/10.1002/2017SW001776

Aa, E., Zou, S., Ridley, A. J., Zhang, S.-R., Coster, A. J., Erickson, P. J., Liu, S., & Ren, J. (2019). Merging of storm-time midlatitude traveling ionospheric disturbances and equatorial plasma bubbles. Space Weather, 17, 285– 298. https://doi.org/10.1029/2018SW002101

Aa, E., Zhang, S.-R., Wang, W., Erickson, P. J., Qian, L., Eastes, R., et al. (2022). Pronounced suppression and X-pattern merging of equatorial ionization anomalies after the 2022 Tonga

volcano eruption. Journal of Geophysical Research: Space Physics, 127, e2022JA030527. https://doi.org/10.1029/2022JA030527

Aa, E., Zhang, S.-R., Liu, G., Eastes, R. W., Wang, W., Karan, D. K., et al. (2023). Statistical analysis of equatorial plasma bubbles climatology and multi-day periodicity using GOLD observations. Geophysical Research Letters, 50, e2023GL103510. https://doi. Org/10.1029/2023GL103510

Aarons, J. (1991). The role of the ring current in the generation or inhibition of equatorial F layer irregularities during magnetic storms. Radio Science, 26(4), 1131–1149. https://doi.org/10.1029/91RS00473

Abdu, M. A., Sobral, J. H. A., de Paula, E. R., & Batista, I. S. (1991). Magnetospheric disturbance effects on the Equatorial Ionization Anomaly (EIA)—An overview. Journal of Atmospheric and Terrestrial Physics, 53, 757–771. https://doi.org/10.1016/0021-9169(91)90126-R.

Abdu, M. A., I. S. Batista, G. O. Walker, J. H. A. Sobral, N. B. Trivedi, and E. R. de Paula (1995), Equatorial ionospheric fields during magnetospheric disturbances: Local time/longitudinal dependences from recent EITS Campaigns, J. Atmos. Sol. Terr. Phys., 57, 1065– 1083.

Abdu, M. A., et al. (2008), Abnormal evening vertical plasma drift and effects on ESF and EIA over Brazil-South Atlantic sector during the 30 October 2003 superstorm, J. Geophys. Res., 113, A07313, doi:10.1029/2007JA012844.

Alken, P., Thébault, E., Beggan, C.D. et al. International Geomagnetic Reference Field: the thirteenth generation. Earth Planets Space 73, 49 (2021). https://doi.org/10.1186/s40623-020-01288-x

Aggson, T. L., Maynard, N. C., Hanson, W. B., and Saba, J. L. (1992), Electric field observations of equatorial bubbles, J. Geophys. Res., 97( A3), 2997– 3009, doi:10.1029/90JA02356.

Anderson, D., and Haerendel, G. (1979), The motion of depleted plasma regions in the equatorial ionosphere, J. Geophys. Res., 84(A8), 4251–4256, doi:10.1029/JA084iA08p04251.

Appleton, E. (1946). Two Anomalies in the Ionosphere. Nature 157, 691. https://doi.org/10.1038/157691a0

Aryal, S., Gan, Q., Evans, J. S., Laskar, F. I., Karan, D. K., Cai, X., et al. (2023). Tongan volcanic eruption induced global-scale thermospheric changes observed by the GOLD mission. Geophysical Research Letters, 50, e2023GL103158. https://doi.org/10.1029/2023GL103158

Balan N., Liu L. B., and Le H. J. (2018). A brief review of equatorial ionization anomaly and ionospheric irregularities. Earth Planet. Phys., 2(4), 257–275. http://doi.org/10.26464/epp2018025

Blanc, M., and Richmond, A. D. (1980). The ionospheric disturbance dynamo. J. Geophys. Res., 85(A4), 1669–1686. https://doi.org/10.1029/JA085iA04p01669

Cai, X., Wang, W., Lin, D., Eastes, R. W., Qian, L., Zhu, Q., et al. (2023). Investigation of the Southern Hemisphere mid-high latitude thermospheric ΣO/N2 responses to the Space-X storm. Journal of Geophysical Research: Space Physics, 128, e2022JA031002. https://doi.org/10.1029/2022JA031002

Cherniak, I., & Zakharenkova, I. (2022). Development of the storm-induced ionospheric irregularities at equatorial and middle latitudes during the 25–26 August 2018 geomagnetic storm. Space Weather, 20, e2021SW002891. https://doi.org/10.1029/2021SW002891

Eastes, R.W., McClintock, W.E., Burns, A.G. et al. (2017), The Global-Scale Observations of the Limb and Disk (GOLD) Mission. Space Sci Rev 212, 383–408, doi:10.1007/s11214-017-0392-2.

Eastes, R. W., S. C. Solomon, R. E. Daniell, D. N. Anderson, A. G. Burns, S. L. England, C. R. Martinis, and W. E. McClintock (2019), Global-scale observations of the equatorial ionization anomaly. Geophysical Research Letters, 46, 9318–9326, https:// doi.org/10.1029/2019GL084199.

493 Eastes, R. W., McClintock, W. E., Burns, A. G., Anderson, D. N., Andersson, L., Aryal, S., et al.
494 (2020). Initial Observations by the Global-scale Observations of the Limb and Disk (GOLD)
495 mission. Journal of Geophysical Research: Space Physics, 125, e2020JA027823.
496 https://doi.org/10.1029/2020JA027823.

497 Eastes, R. W., Karan, D. K., Martinis, C., Daniell, R. E., Gan, Q., Burns, A. G., & McClintock,
498 W. E. (2023). GOLD observations of longitudinal variations in the nighttime equatorial ionization
499 anomaly (EIA) crests' latitudes. Journal of Geophysical Research: Space Physics, 128,
500 e2022JA031007. https://doi.org/10.1029/2022JA031007
501
502 Fejer, B. G., C. A. Gonzales, D. T. Farley, M. C. Kelley, and R. F. Woodman (1979), Equatorial
503 electric fields during magnetically disturbed conditions 1. The effect of the interplanetary
504 magnetic field, J. Geophys. Res., 84 (A10), 5797–5802, doi:10.1029/JA084iA10p05797.
505
506 Ferdousi, B., Nishimura, Y.,Maruyama,N., & Lyons, L. R. (2019). Subauroral neutral wind
507 driving and its feedback to SAPS during the 17March 2013 geomagnetic storm. Journal of
508 Geophysical Research: Space Physics, 124, 2323–2337. https://doi.org/10.1029/2018JA026193
509
510 Gan, Q., Oberheide, J., Goncharenko, L., Qian, L., Yue, J., Wang, W., et al. (2023). GOLD
511 synoptic observations of quasi-6-day wave modulations of post-sunset equatorial ionization
512 anomaly during the September 2019 Antarctic sudden stratospheric warming. Geophysical
513 Research Letters, 50, e2023GL103386. https://doi.org/10.1029/2023GL103386

514 Hanson, W. B., and Moffett, R. J. (1966). Ionization transport effects in the equatorial F region. J.
515 Geophys. Res., 71(23), 5559–5572. https://doi.org/10.1029/JZ071i023p05559
516
517 Huang, C.-S., Zhang, Y., Wang, W., Lin, D., & Wu, Q. (2021). Low-latitude zonal ion drifts and
518 their relationship with subauroral polarization streams and auroral return flows during intense
519 magnetic storms. Journal of Geophysical Research: Space Physics, 126, e2021JA030001.
520 https://doi.org/10.1029/2021JA030001
521

Huba, J. D., Becker, E., & Vadas, S. L. (2023). Simulation study of the 15 January 2022 Tonga event: Development of super equatorial plasma bubbles. Geophysical Research Letters, 50, e2022GL101185. https://doi.org/10.1029/2022GL101185

Hysell, D. L., Kelley, M. C., Swartz, W. E., and Farley, D. T. (1994), VHF radar and rocket observations of equatorial spread F on Kwajalein, J. Geophys. Res., 99(A8), 15065– 15085, doi:10.1029/94JA00476.

Karan, D. K., D. Pallamraju, K. A. Phadke, T. Vijayalakshmi, T. K. Pant, and S. Mukherjee (2016), Electrodynamic influence on the diurnal behavior of neutral daytime airglow emissions, Ann. Geophys., 34, 1019–1030, doi:10.5194/angeo-34-1019-2016.

Karan, D. K., & Pallamraju, D. (2020). On estimation of daytime equatorial vertical (E × B) plasma drifts using optical neutral dayglow emission measurements. Journal of Geophysical Research: Space Physics, 125, e2019JA026775. https://doi.org/10.1029/2019JA026775

Karan, D. K., Daniell, R. E., England, S. L., Martinis, C. R., Eastes, R. W., Burns, A. G., & McClintock, W. E. (2020). First zonal drift velocity measurement of equatorial plasma bubbles (EPBs) from a geostationary orbit using GOLD data. J. Geophys. Res. Space Physics, 125, e2020JA028173, doi:10.1029/2020JA028173

Karan, D. K., Eastes, R. W., Daniell, R. E., Martinis, C. R., & McClintock, W. E. (2023a). GOLD mission's observation about the geomagnetic storm effects on the nighttime equatorial ionization anomaly (EIA) and equatorial plasma bubbles (EPB) during a solar minimum equinox. Space Weather, 21, e2022SW003321. https://doi.org/10.1029/2022SW003321

Karan, D. K., Eastes, R. W., Martinis, C. R., Daniell, R. E., Solomon, S. C., & McClintock, W. E. (2023b). Unique combinations of differently shaped equatorial plasma bubbles occurring within a small longitude range. Journal of Geophysical Research: Space Physics, 128, e2023JA031625. https://doi.org/10.1029/2023JA031625.

553 Kelley, M. C. (2009). Equatorial plasma instabilities and mesospheric turbulence. In The Earth's
554 ionosphere: Plasma physics and electrodynamics (2nd ed., pp. 142–149). MA, USA: Academic
555 Press.
556
557 Kelley, M. C., Makela, J. J., Chau, J. L., and Nicolls, M. J. (2003), Penetration of the solar wind
558 electric field into the magnetosphere/ionosphere system, Geophys. Res. Lett., 30, 1158,
559 doi:10.1029/2002GL016321, 4.
560
561 Kil, H., R. A. Heelis, L. J. Paxton, and S.-J. Oh (2009), Formation of a plasma depletion shell in
562 the equatorial ionosphere, J. Geophys. Res., 114, A11302, doi:10.1029/2009JA014369.

563 Kil, H., W. K. Lee, L. J. Paxton, M. R. Hairston, and G. Jee (2016), Equatorial broad plasma
564 depletions associated with the evening prereversal enhancement and plasma bubbles during the 17
565 March 2015 storm, J. Geophys. Res. Space Physics, 121, 10,209–10,219,
566 doi:10.1002/2016JA023335.

567 Laskar, F. I., Karan, D. K., Daniell, R. E., Codrescu, M. V., Eastes, R. W., Pedatella, N. M., et al.
568 (2024). The X-pattern merging of the equatorial ionization anomaly crests during geomagnetic
569 quiet time. Journal of Geophysical Research: Space Physics, 129, e2023JA032224.
570 https://doi.org/10.1029/2023JA032224

571 Laundal, K. M., and Richmond, A. D. (2017) Magnetic Coordinate Systems, Space Sci Rev, 206,
572 27-59. https://doi.org/10.1007/s11214-016-0275-y
573
574 Lin, C. H., Richmond, A. D., Heelis, R. A., Bailey, G. J., Lu, G., Liu, J. Y., Yeh, H. C., and Su,
575 S. Y. (2005). Theoretical study of the low- and midlatitude ionospheric electron density
576 enhancement during the October 2003 superstorm: Relative importance of the neutral wind and
577 the electric field. J. Geophys. Res., 110(A12), A12312. https://doi.org/10.1029/2005JA011304

578 Makela, J. J., and Kelley, M. C. (2003), Field-aligned 777.4-nm composite airglow images of
579 equatorial plasma depletions, Geophys. Res. Lett., 30, 1442, doi:10.1029/2003GL017106, 8.

580 Manoj, C., and S. Maus (2012), A real-time forecast service for the ionospheric equatorial zonal
581 electric field, Space Weather,10, S09002, doi:10.1029/2012SW000825
582
583 Martinis, C., Eccles, J. V., Baumgardner, J., Manzano, J., & Mendillo, M. (2003). Latitude
584 dependence of zonal plasma drifts obtained from dual-site airglow observations. Journal of
585 Geophysical Research, 108(A3), 1129. https://doi.org/10.1029/2002JA009462

586 Martinis, C. R., Mendillo, M. J., & Aarons, J. (2005). Toward a synthesis of equatorial spread F
587 onset and suppression during geomagnetic storms. Journal of Geophysical Research, 110(A7),
588 A07306. https://doi.org/10.1029/2003JA010362

589 Martinis, C., J. Baumgardner, M. Mendillo, J. Wroten, A. Coster, and L. Paxton (2015), The night
590 when the auroral and equatorial ionospheres converged, J. Geophys. Res. Space Physics, 120,
591 8085–8095, doi:10.1002/2015JA021555.

592 Mendillo, M., and Tyler, A. (1983), Geometry of depleted plasma regions in the equatorial
593 ionosphere, J. Geophys. Res., 88( A7), 5778– 5782, doi:10.1029/JA088iA07p05778.

594 McClintock, W. E., Eastes, R. W., Beland, S., Bryant, K. B., Burns, A. G., Correira, J., et al (2020).
595 Global-scale Measurements of the Limb and Disk (GOLD) Mission Implementation: 2.
596 Observations, Data Pipeline and Level 1 Data Products. Journal of Geophysical Research: Space
597 Physics, 125, e2020JA027809. https://doi.org/10.1029/2020JA027809.
598
599 Ossakow, S. L., and Chaturvedi, P. K. (1978), Morphological studies of rising equatorial spread
600 F bubbles, J. Geophys. Res., 83(A5), 2085–2090, doi:10.1029/JA083iA05p02085.

601 Patra, A. K., P. P. Chaitanya, N. Dashora, M. Sivakandan, and A. Taori (2016), Highly localized
602 unique electrodynamics and plasma irregularities linked with the 17 March 2015 severe magnetic
603 storm observed using multitechnique common-volume observations from Gadanki, India, J.
604 Geophys. Res. Space Physics, 121, 11,518–11,527, doi:10.1002/2016JA023384.

605 Rajesh, P. K., Lin, C. C. H., Lin, J. T., Lin, C. Y., Liu, J. Y., Matsuo, T., et al. (2022). Extreme
606 poleward expanding super plasma bubbles over Asia-Pacific region triggered by Tonga volcano

607 eruption during the recovery-phase of geomagnetic storm. Geophysical Research Letters, 49,
608 e2022GL099798. https://doi.org/10.1029/2022GL099798

609 Sousasantos, J., Gomez Socola, J., Rodrigues, F.S. et al. Severe L-band scintillation over low-to-
610 mid latitudes caused by an extreme equatorial plasma bubble: joint observations from ground-
611 based monitors and GOLD. Earth Planets Space 75, 41 (2023). https://doi.org/10.1186/s40623-
612 023-01797-5

613 Spogli., L, D. Sabbagh, M. Regi, C. Cesaroni, L. Perrone, L. Alfonsi, D. Di Mauro, S. Lepidi, S.
614 A. Campuzano, D. Marchetti, A. Santis, A. Malagnini, C. Scotto, G. Cianchini, Xu Hui Shen, A.
615 Piscini, A. Ippolito, (2021). Ionospheric Response Over Brazil to the August 2018 Geomagnetic
616 Storm as Probed by CSES-01 and Swarm Satellites and by Local Ground-Based Observations,
617 Journal of Geophysical Research: Space Physics, 10.1029/2020JA028368, 126, 2.

618 Sutton, E. K., Forbes, J. M., and Nerem, R. S. (2005), Global thermospheric neutral density and
619 wind response to the severe 2003 geomagnetic storms from CHAMP accelerometer data, J.
620 Geophys. Res., 110, A09S40, doi:10.1029/2004JA010985.
621
622 Takahashi, T., H. Oya, S. Watanabe (1987), Ionospheric disturbances induced by substorm
623 associated electric fields in the low-latitude F-region, J. Geomag. Geoelecric, 39, 187-209,
624 https://doi.org/10.5636/jgg.39.187

625 Thébault, E., Finlay, C.C., Beggan, C.D., Alken, P., Aubert, J., Barroi, O. et al. (2015).
626 International Geomagnetic Reference Field: the 12th generation. Earth Planet Sp 67, 79,
627 https://doi.org/10.1186/s40623-015-0228-9
628
629 Zalesak, S.T., Ossakow, S.L., Chaturvedi, P.K., (1982), Nonlinear equatorial spread F: The effect
630 of neutral winds and background Pedersen conductivity. J. Geophys. Res 87, 151.
631 https://doi.org/10.1029/ 93ja00762.